Toroid Cavity Detectors for High-Resolution NMR Spectroscopy and Rotating Frame Imaging: Capabilities and Limitations

Konstantin I. Momot, Nader Binesh, Olaf Kohlmann, and Charles S. Johnson, Jr.[1]

Department of Chemistry, University of North Carolina, Chapel Hill, North Carolina 27599-3290

The capabilities of toroid cavity detectors for simultaneous rotating frame imaging and NMR spectroscopy have been investigated by means of experiments and computer simulations. The following problems are described: (a) magnetic field inhomogeneity and subsequent loss of chemical shift resolution resulting from bulk magnetic susceptibility effects, (b) image distortions resulting from off-resonance excitation and saturation effects, and (c) distortion of lineshapes and images resulting from radiation damping. Also, special features of signal analysis including truncation effects and the propagation of noise are discussed. B_0 inhomogeneity resulting from susceptibility mismatch is a serious problem for applications requiring high spectral resolution. Image distortions resulting from off-resonance excitation are not serious within the rather narrow spectral range permitted by the RF pulse lengths required to read out the image. Incomplete relaxation effects are easily recognized and can be avoided. Also, radiation damping produces unexpectedly small effects because of self-cancellation of magnetization and short free induction decay times. The results are encouraging, but with present designs only modest spectral resolution can be achieved. © 2000 Academic Press

Key Words: toroid; imaging; rotating frame; radiation damping; diffusion.

INTRODUCTION

Radiofrequency (RF) fields for NMR spectroscopy are usually provided by solenoid or saddle coils. In high-resolution applications, uniformity of B_1 fields and sensitivity are highly desirable, but the choice of coil type is usually dictated by the magnet geometry and spatial restrictions. For example, NMR in superconducting magnets requires that the RF field be polarized perpendicular to the vertical symmetry axis of the magnet. Saddle coils that can accommodate vertical sample tubes are often chosen in spite of the fact that the signal to noise (S/N) ratio is expected to be a factor of 3 lower than for solenoid coils (*1*). The S/N difference results largely from the lower filling factors for samples in saddle coils that is associated with the inefficient use of the flux density. A way around this problem, when high sensitivity is required, is to use a

toroid coil than can efficiently trap the flux and provide reasonable B_1 homogeneity. In fact, toroid coils have been shown to give S/N enhancements of a factor of 4 or better relative to saddle coils, but at the cost of sample handling inconvenience and a small flux cross-section compared with the horizontal space required for the coil (*2, 3*).

There are, of course, very different requirements for RF field gradient spectroscopy. Imaging applications and diffusion measurements require constant B_1 gradients or at least that the amplitude of the RF field be simply related to the spatial position (*4*). The combination of RF gradients with high-resolution NMR typically involves the use of a single-loop transmitter coil to provide the RF gradient, with a saddle coil for homogeneous B_1 pulses and for detection (*5*). This arrangement has been successfully used for NMR microscopy and for diffusion measurements but is limited in the magnitude of gradients that can be produced and the extent of the region where the gradient is approximately constant.

Cylindrical NMR detectors similar to that illustrated in Fig. 1 have some of the properties of toroid coils and provide well-characterized RF gradients (*6*). These devices, known as toroid cavity detectors (TCDs), behave as a continuous array of single loops connected in parallel in contrast to the toroid coils where the loops are in series. The TCD is, thus, a low-inductance device that can be tuned to relatively high frequencies. Furthermore, the amplitude of the RF field is inversely proportional to the distance from the symmetry axis of the cavity. It is interesting to note that the first successful NMR experiment on bulk matter made use of a TCD (*7, 8*).

The following advantages of TCDs have been emphasized: (a) sensitivity is inversely proportional to r (reciprocity principle) (*1*) thus permitting the detection of signals from thin layers close to the central rod (*9*), (b) rotating frame imaging of spin densities and displacements with respect to r is practical and provides high resolution (~20 μm) for small values of r (*10*), (c) TCDs can serve as cells for high-pressure NMR, and (d) the central rod can be electrically isolated from ground so it can serve as an electrode in electrochemistry experiments (*6*). What has not been demonstrated or even claimed is that rotating frame imaging with TCDs is compatible with high-resolution NMR.

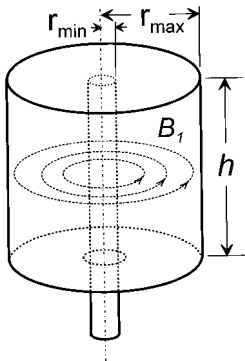[1] To whom correspondence should be addressed. Fax: (919) 962-2388. E-mail: charles_johnson@unc.edu.

FIG. 1. Illustration of a TCD in which the dotted circles represent magnetic field lines.

Since we are interested in chemical applications of TCDs that require both chemical shift resolution and determination of molecular displacement by means of imaging, we have undertaken experiments and computer simulations to investigate the characteristics of these detectors. In this paper we explore the following problems: (a) reduced chemical shift resolution resulting from bulk magnetic susceptibility effects, (b) image distortions resulting from off-resonance excitation and saturation effects, and (c) distortion of lineshapes and images resulting from radiation damping. To anticipate the results, we find that B_0 inhomogeneity resulting from susceptibility mismatch is indeed a serious problem that cannot be eliminated without changing the geometry of the TCD or possibly by using specialized shim stacks. Characteristic image distortions resulting from off-resonance excitation have been obtained both experimentally and theoretically and fortunately are not serious within the rather narrow spectral range permitted by the RF pulse lengths required to read out the image. Also, saturation or incomplete relaxation effects produce image distortions with an easily recognized signature that can be avoided by reducing the repetition rate of the experiment. The predicted effect of radiation damping in experiments involving magnetization gratings consists primarily of winding or unwinding the magnetization helix after the RF preparation pulse; however, this effect was too small to be detected experimentally. In general the results are encouraging, but with the present technology one must be satisfied with modest spectral resolution.

BACKGROUND

RF fields inside TCDs. The TCD is essentially a small copper can with a central conductor insulated from one end and making contact with the other as shown in Fig. 1, i.e., a coaxial detector. The RF field amplitude in the cavity is given by $B_1 = A/r$ where A is the toroid constant, sometimes called the A factor, and r is the distance from the symmetry axis. This permits precisely known phase encoding of the radial position, i.e., an RF pulse produces a Saarinen helix with a pitch pro-

portional to r^2 (*11*). It should be noted that the oscillating RF field is tangential to the circular field lines shown in Fig. 1. At any point we choose the laboratory coordinate frame so that the X axis is also tangential to the field lines and the Y axis is in the radial direction. As with conventional RF coils, the oscillating field is resolved into counterrotating components and only the one rotating with the same sense as the nuclei of interest is retained. The rotating B_1 field then defines the x axis in the rotating frame. Only the rotating coordinate systems with origins in the same radial direction have the same orientation relative to the laboratory frame at a given time. Fortunately, the array of orientations does not introduce any complications in the analysis since the relative orientations of fields and isochromats are identical in all rotating coordinate systems with origins at the same distance from the symmetry axis, i.e., the same value of r.

Imaging with TCDs. The rotating frame imaging (RFI) method makes use of RF field gradients to encode nuclear positions (*4*). Woelk *et al.* have applied this technique to obtain radial images of samples in TCDs (*9*). They have also demonstrated the use of the magnetization grid rotating frame imaging (MAGROFI) method (*12*) to image diffusion in TCDs (*10*). The situation with RFI and MAGROFI differs from pulsed field gradient NMR because the RF pulses both excite the spins and provide the radial gradient for imaging. In MAGROFI (Fig. 2) the first pulse, of length t_{P1}, generates a z-magnetization pattern (after transverse components are eliminated) that is proportional to $\cos[q(r)r]$ where $q(r) = \gamma A t_{P1}/r^2$, thus covering all q space in a single shot. The second RF pulse is incremented in n steps of Δt_{P2}, i.e., $t_{P2} = n\Delta t_{P2}$ with $n = 0$ to $N - 1$, in order to obtain NMR signals with information that characterizes the magnetization pattern or grid present at the end of the diffusion period τ. If t_{P1} is set equal to zero, the second pulse simply images the spin density of the sample as in the RFI experiment.

The free induction decay (FID) obtained for each value of t_{P2} is Fourier transformed with respect to time to obtain the amplitude of the (absorption mode) signal of interest. The signal amplitude versus pulse length, i.e., the interferogram, can be expressed as (*13*)

$$S(t_{P2}) = \int_{r_{min}}^{r_{max}} M_z(r, t_{P1} + \tau) \sin\left(\frac{\gamma A t_{P2}}{r}\right) \cdot \frac{1}{r} \cdot 2\pi rh \, dr. \quad [1]$$

Here $M_z(r, t_{P1} + \tau)$ is magnitude of the z component of
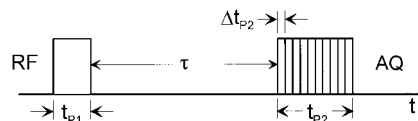

FIG. 2. Pulse sequence for RFI and MAGROFI (see text).

magnetization of the nuclei of interest at the beginning of the pulse P2. Equation [1] represents the transverse component of magnetization integrated over the volume of the sample, here assumed to fill the TCD, taking into account the inverse dependence of sensitivity on the radius. Since the precession frequency of spins in the RF field is given by $\omega_1 = \gamma A/r$, the transformation of variables (r to ω_1) permits Eq. [1] to be recognized as the sine Fourier transform of $r^2 M_z(r, t_{P1} + \tau)$. The image of $M_z(r, t_{P1} + \tau)$ can thus be obtained by dividing the inverse sine transform of $S(t_{P2})$ by r^2.

Effects of radial diffusion and flow. The magnetization grid, that a simple cosinusoidal function of $1/r$ at the end of the first RF pulse, is modified by diffusion, flow, and longitudinal relaxation during the diffusion interval τ. At time $t_{P1} + \tau$ the magnetization at position r is described by (*14*)

$$M_z(r) = M_0[1 - \{1 - \exp(-Dq(r)^2\tau)$$
$$\times \cos[q(r)(r + v(r)\tau)]\}\exp\left(-\frac{\tau}{T_1}\right)]. \quad [2]$$

In Eq. [2] D is the tracer diffusion coefficient, $v(r)$ is the position-dependent radial velocity, and T_1 is the longitudinal relaxation time. We note that $q(r) = 2\pi/\Lambda(r)$ where $\Lambda(r)$ is the local period or wavelength of the grid. Therefore, the scattering vector $q(r)$ is the local tightness of the grid and is responsible for sensitizing the sample to diffusion and flow.

EXPERIMENTAL

Probes for TCD experiments. The basic principles of design of TCDs have been described in the literature (*6*). The TCD used in this work was made of beryllium–copper alloy except for the central rod which was copper. The dimensions defined in Fig. 1 were as follows: $r_{min} = 0.8$ mm; $r_{max} = 7.4$ mm; $h = 24$ mm, wall thickness = 2 mm, and outside height = 30 mm. In anticipation of future use of the TCD in electrophoresis experiments, all interior surfaces were electroplated with silver and the copper rod was isolated from ground by placing two chip capacitors (that were part of the resonance circuit) on top of the TCD. It was found that the arrangement of these capacitors affects the lineshape and achievable shimming quality. Trimmers, required for tuning and matching, were placed as close to the TCD as possible to minimize the stray inductance.

To reduce the effects of susceptibility mismatch, top/bottom inserts were placed inside the cavity. The inserts were 3-mm-thick disks machined from PEEK ($\chi = -9.3$ ppm) (*15*). In some of the test experiments, sample inserts were also introduced to constrain the sample volume (concentric inserts). The inserts were machined of Teflon ($\chi = -10.5$ ppm) or PEEK and typically the radial thickness was 2 to 5 mm.

NMR samples and spectra. ^{1}H spectra were obtained with H_2O/D_2O samples having compositions ranging from 1 to 50% H_2O. D_2O (99.9 atom% D) was obtained from Aldrich Chemical Co., and distilled water was added to prepare the required ratios of H_2O/D_2O.

Image acquisition rates were severely limited by the T_1s of the HDO proton, and relaxation delays of 30 to 60 s were typically required. Copper sulfate (1 mM) was sometimes added to the solutions as a relaxation agent to shorten the T_1 of HDO to approximately 1 s (*16*).

Spectrometer requirements. For imaging applications it is required that the toroid constant A be of the order of 1 mT · mm and that the RF pulse amplitudes remain constant up to 5 ms. All spectra in this work were acquired on a Bruker AC250 spectrometer with a Tecmag computer upgrade. The original RF amplifier provided a maximum of only 30 W and the power output drooped significantly after about 100 μs. These limitations were circumvented by using the low-power output (800 mW) from the Bruker amplifier through a set of attenuators to drive a 150-W power amplifier (AMT M3135). This arrangement provided power stability of better than 1% for 10 ms. The input to the power amplifier was limited to 0.1 mW with a maximum duration of 20 ms by a homemade protection circuit which in turn limited the output power of the amplifier to 40 W to avoid overloading the Bruker RF preamplifier. Fortunately, this level was sufficient to provide an average A factor of 1 mT · mm.

Experimental parameters and data analysis. RF imaging places severe restrictions on the choices of pulse lengths. Consider the problem of imaging a z-magnetization pattern created by an RF pulse of duration t_{P1} and having the form $\cos[q(r)r]$. We must consider both foldover and digital resolution (*17*). According to the Nyquist theorem we must sample at least two times in each period in the pattern to avoid foldover. Therefore, we require that

$$\Delta t_{P2} < \frac{\pi r_{min}}{\gamma A}. \quad [3]$$

To calculate the spatial resolution, we note that in the frequency domain $\delta\nu = 1/t_{P2}$ where $\nu = \omega_1/(2\pi)$. Then by using the relationship $\delta\nu = (\gamma A/2\pi r^2)\delta r$, we find that the resolution is given by

$$\delta r = \frac{2\pi r^2}{\gamma A n \Delta t_{P2}}. \quad [4]$$

Equations [3] and [4] can be combined with $r \approx r_{min}$ to obtain a lower limit on digital resolution close to the rod, $\delta r \geq 2r_{min}/n$. If the resolution is selected to be $\Lambda(r)/2$, Eq. [4] indicates that $t_{P2} = 2t_{P1}$. Digital resolution can, of course, be improved by means of "zero filling" the interferogram prior to the Fourier transformation (*17*).

Taking into account these restrictions, a typical experiment with $A = 1.0$ mT $\cdot$ mm might have $\Delta t_{P2} = 4$ μs and $N = 256$. This combination yields $t_{P2}(\max) = 1$ ms which yields an effective spectral width of the order of 1 kHz. The effects of resonance offset on images are presented under Results and Discussion.

The experimental toroid factor A can be determined from an interferogram obtained with $t_{P1} = 0$. A satisfactory procedure is to use the Levenberg–Marquardt algorithm (18) to obtain a least-squares fit of the experimental interferogram to the right hand side of Eq. [1] with $\tau = 0$. The amplitude and baseline of the interferogram can be included in the fitted parameters. However, the least-squares determination of $r_{\min}$ and $r_{\max}$ is unstable. These parameters should be measured independently and not determined by the fitting procedure.

Another experimental problem is that interferograms often must be truncated, and the way this is done affects the quality of the image. As a general rule, truncating the interferogram at a node, $S(t_{P2}^{\max}) = 0$, is beneficial to the image quality. Also, twofold zero filling of a nonzero terminated interferogram produces significant "beats" in image amplitude, while analogous zero filling of a zero-terminated interferogram preserves the overall quality of the image. Truncation effects are usually less severe in cases where interferograms rapidly decay to zero, e.g., imaging of gratings.

The simulations reported here were performed on a Dell 350 MHz Pentium II PC using the software packages Digital Fortran, Mathcad, and Mathematica.

RESULTS AND DISCUSSION

In RFI the "ideal" interferogram described by Eq. [1] is obtained when RF excitation is the only factor considered. However, in real NMR experiments, factors that distort the interferogram must be taken into account, e.g., inhomogeneity of the static field inside the sample, resonance offset, relaxation, and radiation damping. The effects of these factors on the image and their experimental "signatures" are discussed in this section.

The simulations presented here are based on the Bloch equations. Unless noted otherwise, NMR experiments were simulated in the following way. The rotating frame (x axis defined by $\mathbf{B}_1$) was on resonance and the RF pulses were simulated by simple rotations. During the pulses relaxation, radiation damping, and diffusion were neglected. The free evolution periods were modeled by solving Bloch equations that included any or all of the following: precession in the effective local field, relaxation, diffusion, and radiation damping. Diffusion was modeled using the diffusion propagator (10). Each point of the FID was obtained by integrating the transverse magnetization over the volume of the toroid cavity, and in the construction of an interferogram, only the absorptive part of the Fourier transformed FID was used.

In some of the simulations uniform uncorrelated Gaussian noise (18) was added to the simulated interferogram. The RMS noise, defined as a percentage of the maximum interferogram intensity, was typically 0.5 to 1%. In the image, the noise amplitude is proportional to $1/r^2$ because of the required division by r^2 after Fourier transformation. It should be noted that 0.5% noise in the interferogram noise transforms to 10–20% image noise at $r_{\min}$ and negligible noise at $r_{\max}$, in agreement with experimentally observed images.

Intrinsic B_0 inhomogeneity. When a sample with nonzero magnetic susceptibility is placed in a homogeneous magnetic field, the field inside the sample is inhomogeneous for most sample geometries. This "intrinsic" inhomogeneity is thus a characteristic of the sample and its enclosure. For samples in TCDs we have computed the internal distribution of fields by means of the magnetization surface currents approach (15, 19).

If the TCD and sample are represented by a number of blocks of uniform materials (sample, metal, susceptibility matching plugs), the induced component of the magnetic field can be calculated with Biot–Savart law as shown in Eq. [5]:

$$\mathbf{B}(\mathbf{r}) = \frac{\mu_0}{4\pi} \sum_i \int_{S_i} \frac{\left[\dfrac{B_0(\Delta\chi)_i}{\mu_0} \mathbf{e}_i \times (\mathbf{r} - \mathbf{r}') \right]}{|\mathbf{r} - \mathbf{r}'|^3} d^2r', \quad [5]$$

where S_i is the surface of interface i, $(\Delta\chi)_i$ is the susceptibility difference at interface i, $\mathbf{e}_i$ is a unit vector tangential to the surface of interface i and perpendicular to $\mathbf{B}_0$, and d^2r' spans S_i. In cylindrical coordinates the surface element d^2r' takes the form $R_i(z)d\phi dz$ where $R_i(z)$ is the radius of interface i in cylindrical coordinates and $\mathbf{r}'$ specifies the point $[R_i(z), \phi, z]$. Computationally, various geometries of susceptibility matching plugs can be incorporated in a modular fashion by creating for each interface a subroutine defining its geometry ("surface definition subroutine") and later calling the surface current integration subroutine with the name of the respective surface definition subroutine as a parameter. This approach has been implemented in a Digital FORTRAN program named Toroid__MAP.

Numerical integration of Eq. [5] for the TCD described under Experimental yields the field map for a grid of points in the (r, z) plane that is illustrated in Fig. 3. An analysis of the $\mathbf{B}(\mathbf{r})$ components shows an inhomogeneous distribution of radial and axial components throughout the sample volume. For a D_2O sample, representative values of the quantities describing the induced part of $\mathbf{B}(\mathbf{r})$ are the following: $\langle B_z \rangle = 1850$ Hz, relative standard deviation $\sigma(\langle B_z \rangle) = 0.12$, absolute standard deviation $\sigma(\langle B_r \rangle) = 1400$ Hz, with B expressed in terms of the ^{1}H precession frequency at 5.87 T. The axial components $B_r(\mathbf{r})$ can be neglected in the presence of a large applied field, even though their magnitude has the same order as inhomogeneity of the axial component.

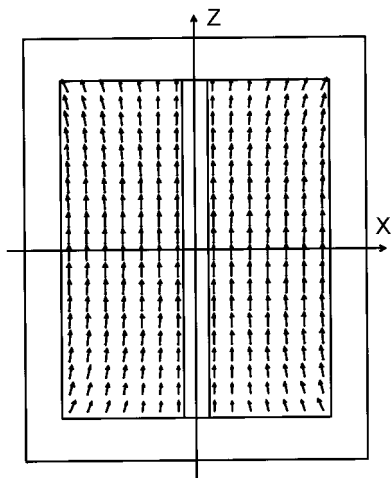When a TCD is used to obtain an NMR spectrum, an RF

FIG. 3. Map of the static magnetic field inside a TCD placed in a homogeneous magnetic field $\mathbf{B}_0$. The external field is parallel to the cylindrical symmetry axis of the TCD.

comparable linewidths, although direct comparison is problematic because of uncertainty as to what set of shims produces a "perfectly homogeneous external field." Unfortunately, the lineshape deteriorates markedly with increasing pulse length.

In view of the successful fitting of $B_z(\mathbf{r})$ with an extensive set of gradients, we undertook the determination of the limits of shimming with known shim functions. The "simulated shimming" procedure is similar to the least-squares expansion of a TCD field map with the following differences. Since the available shim gradients are not cylindrically symmetric, a 3D field map must be constructed from the original 2D field map. Axial symmetry is maintained in the shimmed field distribution only through the effect of combinations of gradients on the 3D map.

The map of the "shimmed" field is given by the residues of the least-squares fitting procedure. This procedure determines the best possible shimming with our spectrometer because the basis set contains only the standard set of shim gradients of a Bruker AC250 instrument (which includes all except the last four gradients listed in Table 2.1, Ref. (*20*)). The unshimmed

pulse first generates a pattern of transverse magnetization components throughout the sample. In the presence of intrinsic inhomogeneity the FID depends on the amount of transverse magnetization associated with each value of the local magnetic field. Therefore, the FID and the resulting lineshape depend on both the duration of the RF pulse and the distribution of static fields. The simulations presented here permit the NMR lineshape for a particular TCD and sample to be obtained as a function of the RF pulse length. The complete simulation requires the convolution of the weighted frequency distribution with a Lorentzian function having the appropriate T_2 value. In the interest of computational efficiency we have chosen to approximate the distribution of local frequencies with a polynomial expansion prior to the convolution.

We note that the cylindrically symmetric $B_z(\mathbf{r})$ distribution can be represented analytically by a set of gradients containing even powers of z and all powers of r. Such an expansion can be performed using, among other methods, the generalized least-squares approach (*18*). In this work, we used the direct product of $\{1, r, \ldots r^4\}$ and $\{1, z^2, \ldots .z^{10}\}$ as the basis set for expanding the TCD field maps. This basis set provides good numerical accuracy (RMS < 0.7 Hz) and is sufficiently compact to be practical in lineshape calculations. The expansion of $B_z(\mathbf{r})$ shows that the most important gradients describing its inhomogeneity are $+r^2$ and $-z^2$.

The simulated lineshape is essentially a histogram of local magnetic fields weighted by the local transverse magnetization density and convoluted with a Lorentzian shape function. Figure 4a shows the lineshape simulated for an unshimmed $H_2O/$ D_2O (1:99) sample acquired with a 4 μs RF pulse ($A = 1.0$ mT · mm, $T_2 = 1.0$ s). The inhomogeneity of $B_z(\mathbf{r})$ gives rise to an unsymmetric lineshape with widths at half-height and 0.1 height of $\Delta\nu_{0.5} = 20$ Hz and $\Delta\nu_{0.1} = 330$ Hz, respectively. Experimentally recorded spectra of unshimmed samples have
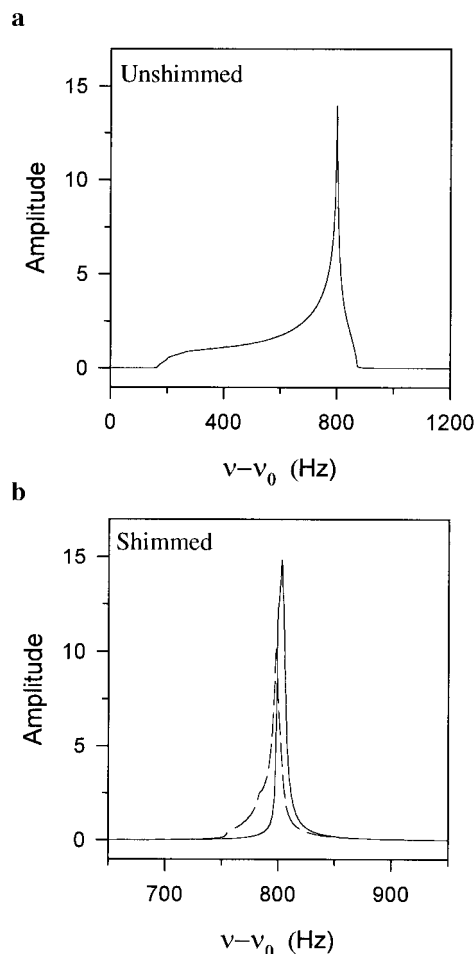

FIG. 4. Lineshape of the TCD sample: (a) without shimming; (b) after perfect shimming (solid line) and with slightly mismatched shims (dashed line) with $t_P = 4$ μs.
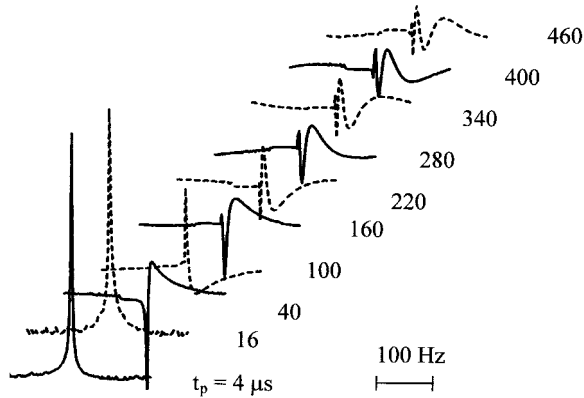
FIG. 5. Lineshape of the TCD sample in the presence of slightly mismatched shims for a series of t_P values.

$$M_x = M_0 \sin(2\theta_e)\sin^2(\omega_e t/2)$$

$$M_y = M_0 \cos(\theta_e)\sin(\omega_e t)$$

$$M_z = M_0[1 - 2\cos^2(\theta_e)\sin^2(\omega_e t)], \qquad [6]$$

where $\tan\theta_e = \delta/\omega_1$, $\omega_e = (\omega_1^2 + \delta^2)^{1/2}$, $\omega_1 = \gamma B_1$, $\delta = \gamma B_0 - \omega$, and ω is the angular frequency of the rotating coordinate system. For a sample in a TCD, Eq. [6] describes the precession of the magnetization (at a particular radial position r) in a cone around the effective magnetic field $\mathbf{H}_{\text{eff}} = (A/r)\mathbf{i} + (\delta/\gamma)\mathbf{k}$. Since the angle between $\mathbf{H}_{\text{eff}}$ and the z axis decreases as r increases, there are nonlinear changes in the amplitude and phase of M_y and a resulting distortion in the image.

An interferogram obtained off-resonance is given by

$$S_y(t_{P2}) = 2\pi h \int_{r_{\min}}^{r_{\max}} \frac{1}{\sqrt{1 + (r\delta/\gamma A)^2}}$$

$$\times \sin\left[\frac{\gamma A t_{P2}}{r}\sqrt{1 + (r\delta/\gamma A)^2}\right] dr. \qquad [7]$$

This equation permits the criteria for off-resonance distortion to be established. In the limit of small offset, the radical in the denominator can be expanded to obtain the following condition for accurate amplitude: $r_{\max}\delta/(\gamma A) \ll 1$. The second criterion, resulting from the expansion of the radical in the argument of the sine function, reduces to $\delta < 2\pi/t_{P2}$, a criterion already imposed by spectral width restrictions.

Experimental and simulated images obtained with offset frequencies ranging from 0 to 5 kHz are shown in Figs. 6a and 6b, respectively. There is good agreement between these results, and we note that the parabolically rising roof of the image and the underestimation of $r_{\max}$ are experimental signatures of off-resonance irradiation. The retraction or shrinkage of the image is a consequence of the increase in precession frequency that results from the contribution of the offset term to H_{eff}. An inspection of the phase angle in Eq. [7] shows that the effective value of $r_{\max}$ becomes $r_{\max}/[1 + (r_{\max}\delta/\gamma A)^2]^{1/2}$. The fractional increase is significant for larger values of r and results in mapping of the intensity to lower r values in the image. This becomes apparent after introducing a new integration variable, $l = r/[1 + (r\delta/\gamma A)^2]^{1/2}$, and evaluating the new differential. For $(r\delta/\gamma A)^2 \ll 1$, the intensity of the image behaves as $1 + (r\delta/\gamma A)^2$.

A hidden danger regarding determination of the toroid constant A from off-resonance images should be noted. The A factor serves as a scaling factor for the r domain. Because the apparent $r_{\max}$ is underestimated in off-resonance images, the A factor based on such images will be overestimated in the least-squares procedure mentioned under Experimental. Therefore, interferograms obtained on or near resonance must be used to determine A unless the analysis is based on Eq. [7].
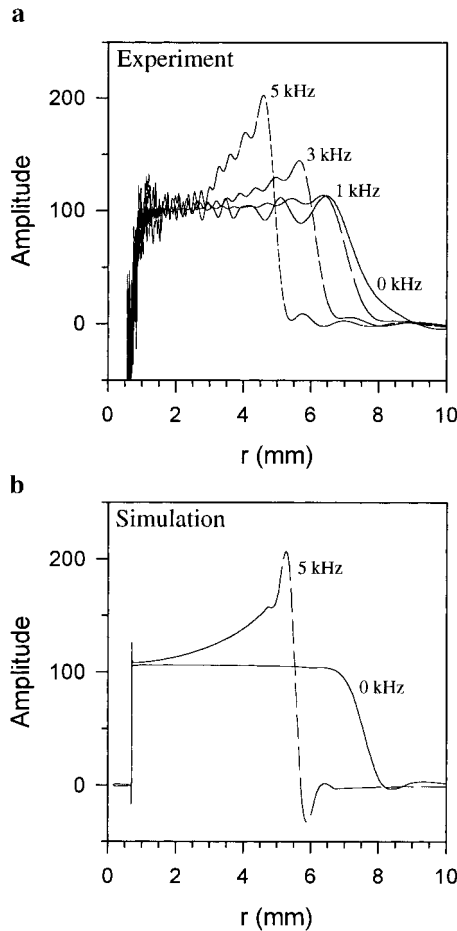
and shimmed lineshapes are shown in Figs. 4a and 4b, respectively, with different frequency scales. The solid line in Fig. 4b shows the theoretical limit of the shimming corresponding to the global minimum of χ^2 in the least-squares procedure. This lineshape has the width at half-height of $\Delta\nu_{0.5} = 8$ Hz and at 0.1 height of $\Delta\nu_{0.1} = 20$ Hz. The dashed line is a result obtained with slightly mismatched shims. The latter spectrum features a narrow central component with wide inhomogeneous "wings"—an observation described previously in the literature (13).

Figure 5 shows the simulated lineshape of a TCD sample in the presence of small static field inhomogeneities for a series of values of RF pulse length, t_P. These lineshapes were obtained by integrating the Bloch equations followed by Fourier transformation. The inhomogeneity of the static magnetic field was defined analytically as $\alpha r^6 - \beta z^6$, where α and β were set so that the range of the values of the two terms were from 0 to 72 Hz and from 0 to -56 Hz, respectively. These gradients qualitatively describe the field map distortions that remain in the sample after a "perfect" or "near-perfect" shimming.

As can be seen from Fig. 5, the lineshape closely resembles a Lorentzian function at a small t_P (4 μs). However, as t_P is increased, the signal first appears to be dephased and then breaks up. This behavior, which has been observed in all of the RFI experiments performed in this laboratory, presents a severe problem for high-resolution NMR with the TCD. A signal with an acceptable linewidth (several Hz for H̲DO) at small values of t_P may broaden by an order of magnitude or more when large t_P values are used. The breakup of the signal does not affect the interferogram obtained by integration of the signal intensity; however, accurate integration may not be possible in all circumstances.

Effects of off-resonance excitation on the image. Analytical solutions are easily obtained for the Bloch equations when relaxation and diffusion are neglected during the RF pulse (21). In the notation of Madhu and Kumar the solutions are (22)

FIG. 6. (a) Experimental and (b) simulated images of a uniform TCD sample for various resonance offset frequencies.

FIG. 7. Experimental (a–c) and simulated images (d–f) of a uniform TCD sample with various T/T_1 ratios.

Effect of incomplete longitudinal relaxation on the image. Thus far we have assumed that the relaxation delay after the FID is acquired in imaging experiments is much longer than T_1. When that is not the case, nonlinear effects lead to severe distortions of image. An extreme example is shown in Fig. 7c. The obvious steps in this image occur at r_{max}/n where $n = 1$, 2, 3, . . . In the frequency domain prior to transforming to r, we find that the steps are evenly spaced, suggesting the introduction of harmonics.

We have simulated the following on-resonance imaging experiment with t_{P1}, $\tau = 0$. The FID is acquired in a single transient, the delay between RF pulses is T, and the RF pulse length t_{P2} is incremented by Δt_{P2} as illustrated in Fig. 8. We neglect relaxation and diffusion during the RF pulses, and during the delay T we assume that only longitudinal relaxation and diffusion are important. The nth RF pulse (P2) has the duration $n\Delta t_{P2}$, and we define the r-dependent wavevector at the end of the nth pulse as $q_n(r) = \gamma A n \Delta t_{P2}/r^2$ so that the phase angle resulting from the nth pulse is $q_n(r)r$. The cumulative effect of relaxation and diffusion on the acquired signals
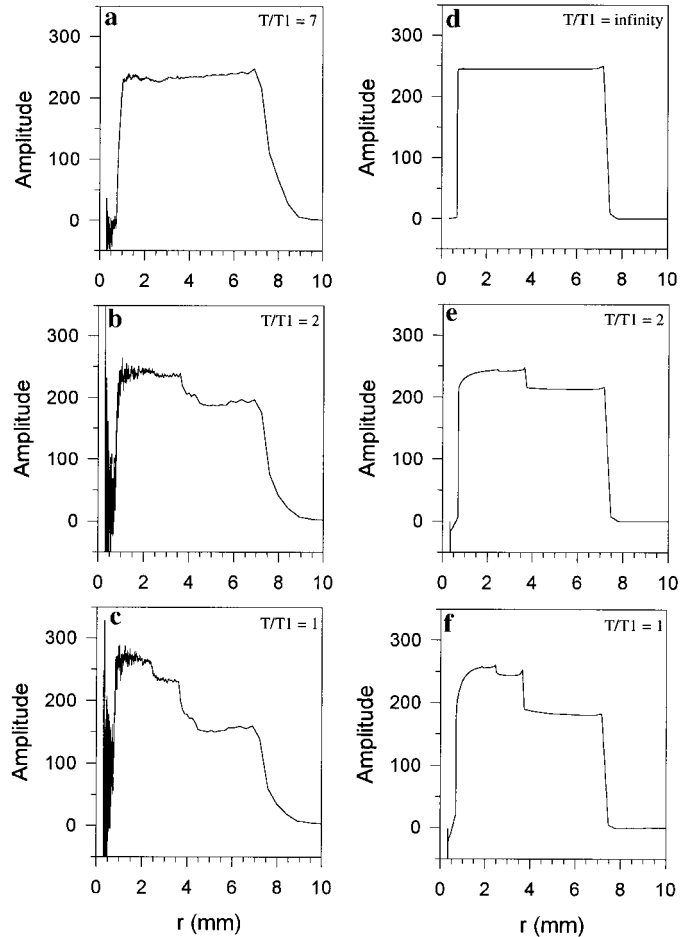
in this experiment on a sample with uniform magnetization M_0 can be described by the following iterative scheme (*10, 12*):

$$f_0(r) = M_0$$
$$C_n(r) = \cos[q_n(r) \cdot r]\exp[-Dq_n^2(r)T]$$
$$f_{n+1}(r) = M_0 + [f_n(r)C_{n+1}(r) - M_0]\exp(-T/T_1). \quad [8]$$

We interpret Eqs. [8] as follows. The first RF pulse prepares a magnetization helix, the transverse components of which
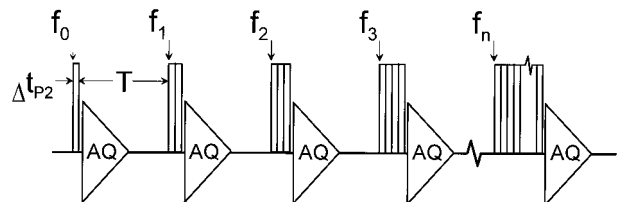

FIG. 8. The pulse sequence for RFI with pulse spacing T and incremented t_{P2} values.

contribute to an FID that provides the first point in the interferogram. A z-magnetization pattern is also prepared, and, if T is not much larger than T_1, a residual pattern remains at the beginning of the second RF pulse. The residual pattern is propagated by successive RF pulses as shown by the function $f_n(r)$, and the points of the interferogram are given by

$$S_n = 2\pi h \int_{r_{\min}}^{r_{\max}} f_{n-1}(r)\sin[q_n(r) \cdot r]dr. \qquad [9]$$

The resulting interferogram suffers nonlinear but periodic distortions since the rate of recovery of magnetization after an RF pulse depends on the deviation from the equilibrium value. An image simulated with recursive scheme [8] with $T/T_1 = 1.0$ is shown in Fig. 7f. In general the effects of diffusion and transverse relaxation (during T) on the image are not significant.

The experimental signature of incomplete longitudinal relaxation is the appearance of descending "steps" in the image. At $T/T_1 = 5$, the steps are negligibly small compared to the image intensity while at $T/T_1 < 1$, the steps are profound. We find that the number of distinguishable steps ranges from 1 ($2 < T/T_1 < 5$) to 3 ($T/T_1 < 1$).

Radiation damping. Effects of radiation damping on NMR signal have been studied extensively for the solenoid and saddle coil detectors (23–27). The essence of the effect is that the FID current in the detector coil induces the feedback magnetic field, $\mathbf{B}_{rd}$, which oscillates with the precession frequency of the spins but has a $\pi/2$ phase delay. Interaction of the magnetic moment of the spins with the feedback field leads to the radiation damping term in the Bloch equations:

$$\left(\frac{d\mathbf{M}}{dt}\right)_{rd} = \gamma[\mathbf{M} \times \mathbf{B}_{rd}]. \qquad [10]$$

The explicit form of the damping term can be derived by the approach of Bloom (24). After a RF pulse of length t_{P1}, the current induced in the circuit is proportional to the precessing magnetization or FID. On resonance and considering only radiation damping effects we have:

$$\text{FID}(t) = kM_0 \frac{\int_{r_1}^{r_2} \sin\theta(r,t)dr}{r_2 - r_1}, \qquad [11]$$

where k is a proportionality constant and $\theta(r, 0) = \gamma At_{P1}/r$. The effective B_1 field resulting from radiation damping is proportional to $-\text{FID}(t)/r$; and since FID(0) can be either positive or negative this field acts to wind or unwind the magnetization helix created by the winding pulse (P1) in the MAGROFI experiment. The winding or unwinding proceeds

until the FID(t) reaches the node of the interferogram nearest to the starting point in the indicated direction.

In a saddle coil detector, where the RF power is approximately uniform, radiation damping drives magnetization to the thermal equilibrium at every point in the sample. The uniformity of magnetization allows one to view radiation damping as being driven by local *transverse magnetization* rather than by the FID. This approximation is reflected in the commonly cited form of radiation damping terms of the Bloch equations (25, 26), but is invalid for TCDs because the RF field is not uniform. As a result, the magnetization at any given point of the TCD can be driven *past* thermal equilibrium.

Another particularity of radiation damping in the TCD concerns the stability of Eq. [10] with a vanishing initial FID. With a saddle coil or solenoid coil radiation damping is present following a "perfect" π pulse because of the FID generated by thermal noise (26, 28). Therefore, inverted magnetization is unstable in the presence of radiation damping. This situation with the TCD is somewhat analogous since every other node of the FID constitutes a stable point. Finally, with the same sample and the same detector, a tight grating will be affected by radiation damping to a lesser extent than a loose grating because the FID is essentially self-canceling for tight gratings. Here the "tightness" of a grating refers to the number of periods of oscillation occurring between $r_{\min}$ and $r_{\max}$, a number proportional to γAt_{P1}. These observations apply not only to the TCDs, but to any RFI detector (5, 29).

In order to assess the effects of radiation damping on spectra and images obtained with TCDs, we have performed two experiments. In the first experiment, spectra were recorded for a series of H_2O/D_2O mixtures with compositions ranging from 1 to 50% H_2O in D_2O. Each spectrum was recorded with a 4-μs RF pulse ($A \approx 1$ mT · mm), and the linewidth of the HDO signal was measured. All widths were in the range 7 ± 1 Hz and no significant correlation was found between the linewidth and concentration of H_2O.

The second experiment was designed to test the effect of radiation damping on a loose grating prepared in a sample of 10% H_2O in D_2O that completely filled the cavity. In this experiment the grating was wound with an RF (winding) pulse of length slightly greater than that required to produce the maximum intensity FID. Since the FID immediately after the pulse was positive, radiation damping should cause the grating to unwind. The control image was acquired following a very short evolution period (20 μs) to ensure that no significant unwinding could occur. The experiment was then repeated with the same length winding pulse but with a much longer evolution period (220 ms). The largest effects are expected at small values of r, and if radiation damping was present, the grating observed in the latter experiment should not be as tight as the control.

The imaging experiment may be more sensitive to RD effects than the linewidths, since the unwinding experiment requires only that the grating be driven a few percent of the internode distance during the longer diffusion delay. Our use of
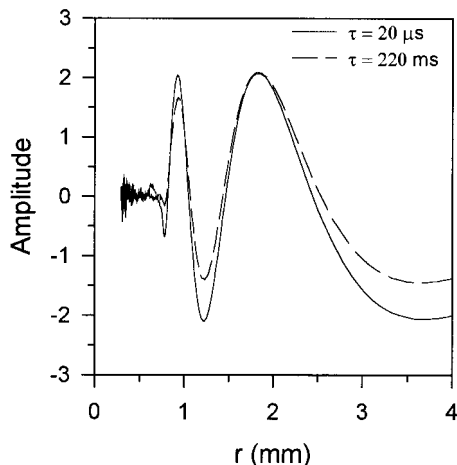
FIG. 9. Grating images for a sample containing 10% H_2O/90% D_2O. Unwinding of magnetization grating with $\tau = 20$ μs (solid line) and 220 ms (dashed line) in a MAGROFI experiment.

a concentrated water sample and a winding pulse that produces close to the maximum intensity FID ensures larger RD effects than would be encountered in typical diffusion measurements. In addition, loose gratings which coexist with large FIDs have small $q(r)$ values and are not affected by diffusion even during a long evolution delay. It should be noted that the imaging part of this experiment is not affected by radiation damping because the points in the interferogram are acquired by integrating over the signal after Fourier transformation [26].

The detector used in the unwinding experiment had an A factor of 0.861 mT · mm and a Q value of 120, both typical of currently available TCDs. As can be seen from Fig. 9, the two acquired gratings have the same tightness, indicating that radiation damping was negligible. The offset of the baselines of the gratings is a consequence of T_1 relaxation during τ. The absence of radiation damping effects is surprising with such a large magnetization especially since the filling factor is unity and Q is fairly large. We invoke three factors to explain the absence of observable radiation damping in TCD experiments. The first factor is the self-cancellation of the FID resulting from a helix of magnetization. The maximum FID amplitude relative to that obtained with a hypothetical uniform $\pi/2$ pulse depends on the ratio r_2/r_1 but was approximately 0.6 in our experiments, and we note that self-cancellation becomes more complete as the RF pulse length is increased. The second factor is stray inductance in the RF circuit that reduces the feedback field inside the TCD, and the third factor is the rapid dephasing of transverse magnetization caused by inhomogeneities in the static magnetic field. Figure 4 demonstrates that the longest achievable T_2^* with our TCD is of the order of 100 ms. Therefore, only radiation damping with shorter characteristic times can be observed. Improvements in TCD design will likely lead to stronger radiation damping effects as increased A factors and improved homogeneity give rise to more intense and slower decaying FIDs.

CONCLUSIONS

In evaluating TCD NMR we have investigated static field inhomogeneities, off-resonance irradiation, saturation (incomplete relaxation) during imaging, and radiation damping. Of these factors, static field inhomogeneity, which causes the NMR signal to "break up" under the long RF pulses, presents the biggest challenge to the use of TCD in imaging applications requiring high spectral resolution. The breakup adversely affects spectral resolution through line broadening and apparent dephasing. Potential ways of handling this problem include susceptibility matching, changing the geometry of the sample in the direction of either a long cylinder or a sphere [13], developing specialized shim coils, or application of reference deconvolution [30]. Off-resonance behavior of magnetization does not present a serious problem for imaging, because the effective spectral width is already limited by the longest imaging pulse. Incomplete relaxation can lead to significant image distortions, but is easily identified and avoided. Radiation damping is not a significant problem with current TCDs but may become severe as the static field homogeneity and the A factor are improved. In this case, radiation damping can have adverse effects on diffusion measurements since it affects the tightness of magnetization grating.

With current technology, we were able to obtain good-quality images from species separated by 400 to 500 Hz. However, imaging species separated by less than 200 Hz is problematic because of overlap of distorted signals. Efficient procedures for data collection and analysis in TCD diffusion experiments and a detailed derivation of radiation damping for TCDs will be presented elsewhere.

REFERENCES

1. D. I. Hoult and R. E. Richards, The signal-to-noise ratio of the nuclear magnetic resonance experiment, *J. Magn. Reson.* **24,** 71 (1976).

2. T. E. Glass and H. C. Dorn, B_1 and B_0 homogeneity considerations for a toroid-shaped sample and detector, *J. Magn. Reson.* **51,** 527 (1983).

3. T. E. Glass and H. C. Dorn, A high sensitivity toroid detector for ^{17}O NMR, *J. Magn. Reson.* **52,** 518 (1983).

4. D. I. Hoult, Rotating frame zeugmatography, *J. Magn. Reson.* **33,** 183 (1979).

5. D. Canet, Radiofrequency field gradient experiments, *Prog. NMR Spectrosc.* **30,** 101 (1997).

6. J. W. Rathke, R. J. Klingler, R. E. Gerald, II, K. W. Kramarz, and K. Woelk, Toroids in NMR spectroscopy, *Prog. NMR Spectrosc.* **30,** 209 (1997).

7. E. M. Purcell, H. C. Torrey, and R. V. Pound, Resonance absorption by nuclear magnetic moments in a solid, *Phys. Rev.* **69,** 37 (1946).

8. R. V. Pound, From radar to nuclear magnetic resonance, *Rev. Mod. Phys.* **71,** S54 (1999).

9. K. Woelk, J. W. Rathke, and R. J. Klingler, Rotating-frame NMR microscopy using toroid cavity detectors, *J. Magn. Reson.* **105,** 113 (1993).

10. K. Woelk, R. E. Gerald, II, R. J. Klingler, and J. W. Rathke, Imaging diffusion in toroid cavity probes, *J. Magn. Reson. A* **121,** 74 (1996).

11. T. R. Saarinen and C. S. Johnson, Jr., Imaging of transient magnetization gratings in NMR: Analogies with laser induced gratings and applications to diffusion and flow, *J. Magn. Reson.* **78,** 257 (1988).

12. R. Kimmich, B. Simon, and H. Kostler, Magnetization-grid rotating-frame imaging technique for diffusion and flow measurements, *J. Magn. Reson. A* **112,** 7 (1995).

13. K. Woelk, J. W. Rathke, and R. J. Klingler, The Toroid Cavity NMR detector, *J. Magn. Reson. A* **109,** 137 (1994).

14. B. Simon, R. Kimmich, and H. Kostler, Rotating-frame-imaging technique for spatially resolved diffusion and flow studies in the fringe field of RF probe coils, *J. Magn. Reson. A* **118,** 78 (1996).

15. F. D. Doty, G. Entzminger, and Y. A. Yang, Magnetism in high-resolution NMR probe design. I: General methods, *Concepts Magn. Reson.* **10,** 133 (1998).

16. N. Bloembergen, E. M. Purcell, and R. V. Pound, Relaxation effects in nuclear magnetic resonance absorption, *Phys. Rev.* **73,** 679 (1948).

17. A. G. Marshall and F. R. Verdun, "Fourier Transforms in NMR, Optical, and Mass Spectroscopy: A User's Handbook," Elsevier, Amsterdam (1990).

18. W. H. Press, S. A. Teukolsky, W. T. Vetterling, B. P. Flannery, "Numerical Recipes in FORTRAN," Cambridge Univ. Press, New York (1992).

19. E. M. Purcell, "Berkeley Physics Course Vol. 2—Electricity and Magnetism," McGraw–Hill, New York (1973).

20. W. W. Conover, Practical guide to shimming superconducting NMR magnets, *In* "Topics in Carbon-13 NMR Spectroscopy, Vol. 4" (G. C. Levy, Ed.), p. 37, Wiley–Interscience, New York (1976).

21. I. I. Rabi, N. F. Ramsey, and J. Schwinger, Use of rotating coordinates in magnetic resonance problems, *Rev. Mod. Phys.* **26,** 167 (1954).

22. P. K. Madhu and A. Kumar, Direct Cartesian-space solutions of generalized Bloch equations in the rotating frame, *J. Magn. Reson. A* **114,** 201 (1995).

23. N. Bloembergen and R. V. Pound, Radiation damping in magnetic resonance experiments, *Phys. Rev.* **95,** 8 (1954).

24. S. Bloom, Effects of radiation damping on spin dynamics, *J. Appl. Phys.* **28,** 800 (1957).

25. W. S. Warren, S. L. Hammes, and J. L. Bates, Dynamics of radiation damping in nuclear magnetic resonance, *J. Chem. Phys.* **91,** 5895 (1989).

26. X. A. Mao and C. H. Ye, Understanding radiation damping in a simple way, *Concepts Magn. Reson.* **9,** 173 (1997).

27. A. Abragam, "The Principles of Nuclear Magnetism," Oxford Univ. Press, London (1961).

28. A. Sodickson, W. E. Maas, and D. G. Cory, The initiation of radiation damping by noise, *J. Magn. Reson. B* **110,** 298 (1996).

29. R. Kimmich, "NMR Tomography, Diffusometry, and Relaxometry," Springer, Berlin (1997).

30. G. A. Morris, H. Barjat, and T. J. Horne, Reference deconvolution methods, *Prog. NMR Spectrosc.* **31,** 197 (1997).